Chinese Journal of Chemical Engineering 83 (2025) 38–50

Contents lists available at ScienceDirect

Chinese Journal of Chemical Engineering

journal homepage: www.elsevier.com/locate/CJChE

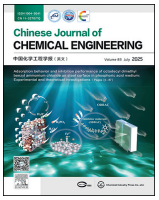

Full Length Article

Ultrasonic-assisted rapid liquid-phase exfoliation of MFI-type zeolite nanoparticle aggregates

Xinyi Gao, Qiancheng Zheng, Zhengbao Wang *

Key Laboratory of Biomass Chemical Engineering of Ministry of Education, ERC of Membrane and Water Treatment (MOE), College of Chemical and Biological Engineering, Zhejiang University, Hangzhou 310058, China

ARTICLE INFO

Article history:
Received 9 December 2024
Received in revised form
7 January 2025
Accepted 18 February 2025
Available online 24 April 2025

Keywords:
Nanoparticles
Zeolite
Liquid phase exfoliation
Ultrasonic-assisted
Vacuum freeze drying
Sintering

ABSTRACT

The preparation of dispersible MFI-type zeolite nanoparticles with open micropores is challenging. Herein, a rapid and effective ultrasound-assisted liquid-phase exfoliation method along with a freeze-drying process for redispersion of calcined silicalite-1 (S-1) zeolite nanoparticle aggregates using 3-aminopropanol as an exfoliating agent is demonstrated. The exfoliation of S-1 zeolite nanoparticles is characterized by X-ray diffraction, scanning electron microscopy and DLS particle size analysis. The effects of drying methods of as-synthesized zeolite nanoparticle suspension, zeolite contents in frozen nanoparticle suspension, exfoliating agent concentrations, and zeolite doses in ultrasonic suspension on exfoliation efficiency are systematically investigated. It is found that the S-1 zeolite nanoparticle (~70 nm) achieves a yield up to 95% through a 30 min ultrasonic exfoliation in a 3-aminopropanol solution along with a freeze-drying process. The proposed exfoliation mechanism involves two primary stages: guest molecule insertion followed by water expansion, both substantially enhanced by tip sonication. This work offers a comprehensive understanding of the exfoliation process, provides valuable insights into the dispersion of sintered zeolite nanoparticles.

1. Introduction

The synthesis of nanoscale zeolite has attracted considerable interest, as reducing crystal size to the nanometer scale imparts several advantageous properties, including a large specific surface area, high stability in suspension, shorter diffusion paths, and a greater number of exposed active sites compared to their micron-sized counterparts [1–7]. These features are advantageous not only in heterogeneous catalysis and molecular separation [8–11], but also expand their potential for emerging fields, including chemical sensing [12–14], optical devices [15,16], biomedical and biological analyses [17], as well as applications in mixed matrix membranes (MMMs). For instance, Gutiérrez-Rubio *et al.* [18] addressed the issue of poor activity in micron-sized zeolite catalysts for vapor-phase acetylation reactions by introducing additional mesopores into nano-MFI zeolites using a hard templating method. Chuah *et al.* [19] synthesized nanoscale silicalite-1 (S-1), ETS-10, and SAPO-34 zeolites and then dispersed them in a chloroform solution in order to prepare the MMMs. This approach enhances gas molecule adsorption and diffusion, significantly improving the CO_2/N_2 selectivity. Moreover, the use of NaX zeolite nanoparticles led to an improvement in the selectivity of CO_2/N_2 and O_2/N_2 in Pebax-1657/zeolite NaX MMMs [20]. On the one hand, ascribing to leveraging the selective adsorption properties and abundant micropore volume of the zeolite nanoparticles, both studies mentioned above have surpassed the Robertson upper limit of conventional polymer membranes. On the other hand, the presence of zeolite nanoparticles can restrict the movement of polymer chains, increasing the rigidity of the polymer matrix near the zeolite surface. These significant achievements promote the practical application of zeolite nanoparticles.

MFI-type zeolite nanoparticles are highly valued in catalysis and environmental applications due to their enhanced catalytic activity, high surface area, and low diffusion resistance, making them ideal candidates for a wide range of industrial processes, including hydrocarbon transformations and pollutant removal [21–23]. Various strategies have been investigated for preparing nanoscale zeolites. Zhang *et al.* [24] obtained ~200 nm S-1 zeolites within 10 min at 200 °C with the assistance of seeds. Afterwards, Grand *et al.* [25] reported the one-pot synthesis of silanol-free nanosized MFI-type zeolites by introducing atomically dispersed tungsten. The W–O–Si bonds exhibit greater stability than the Si–O–Si bonds

* Corresponding author.
E-mail address: zbwang@zju.edu.cn (Z. Wang).

https://doi.org/10.1016/j.cjche.2025.02.029

found in all-silica MFI zeolites. Recently, it is widely accepted that the lower water content plays an important role in a more supersaturated composition, which in turn accelerates the nucleation and growth of zeolite crystals, resulting in a significant reduction in reaction time and particle size. Xiao *et al.* [26] synthesized 100–200 nm ZSM-5 zeolites, demonstrating that higher nutrient gel concentrations ($H_2O/SiO_2 = 2$) greatly affect the crystal morphology and size. Nonetheless, a disadvantage of this approach is that the product often exists in the form of small crystal aggregates. Zhang *et al.* [27] also demonstrated an amino acid-assisted synthetic approach to synthesize MFI zeolite nanocrystals by two-step crystallization in a concentrated gel system. These studies provide an in-depth understanding of the formation mechanism of zeolite nanocrystals, guiding future research on zeolite synthesis.

Organic structure-directing agents (OSDA) are usually required to reduce the zeolite crystal size [28]. The nanocrystals so obtained contain OSDA in their intrinsic micropores, and the OSDA has to be removed for many applications [8,16,19], which is often achieved by calcination, leading to aggregation. The aggregation of zeolite nanocrystals is a significant hurdle for their practical applications [29]. In response to this issue, some research has been focused on the exfoliation of zeolite crystals. For example, an organic polymer network as a temporary barrier during calcination was used to prevent zeolite nanocrystal aggregation [30]. Surface functionalization or coating of zeolite nanoparticles with organic silane reagents has also been reported as a strategy to reduce aggregation. Li *et al.* [31] dispersed 100 nm LTA zeolite by utilizing sulfonated polyethersulfone as a prime in MMMs. The hydrophilicity of sulfonic acid groups enhances interactions between zeolite particles. When negative charges coat the zeolite surface, electrostatic repulsion occurs between particles, improving their dispersion. The nanosized MFI zeolite was functionalized with ethoxydimethylphenylsilane to enhance its anti-aggregation properties. The particle size remained almost unchanged, increasing by only 37% after 10 d. Compared to the unfunctionalized zeolite, the functionalized version showed a 20% decrease in specific surface area and a 40% decrease in external surface area, while the micropore volume remained relatively stable [32]. However, these processes are not very environmentally friendly. Therefore, the preparation of dispersible MFI-type zeolite nanoparticles with open micropores is still a challenge.

The exfoliation of two-dimensional (2D) materials, including 2D zeolites, such as the MWW [33,34], MFI [35], and RWR [36] frameworks and so on, has been well investigated. One of the most prominent exfoliation techniques uses tetrabutylammonium hydroxide (TBAOH), which has been demonstrated to effectively exfoliate zeolites like MWW and MFI into nanosheets with a high yield, showing significant potential for practical applications [33,35,37]. The TBA^+ cations occupy the interlayer regions, causing osmotic swelling that increases the distance between the layers. Concurrently, the hydroxide ions (OH^-) disrupt interlayer interactions, which weakens the structural integrity of the material, thereby further aiding in exfoliation. For instance, colloidal suspensions of MWW monolayers could be produced directly by stirring 0.5 g MCM-56 with 3% to 5% TBAOH solutions, and the yield is 40% [33]. In addition, it is worth mentioning that the solvent-mediated freeze-thaw exfoliation of SAPO-34 nanosheets [38]. The material begins by introducing *n*-hexane into the zeolite interlayers, then is rapidly frozen in liquid nitrogen, utilizing the shear force from the volume expansion of solvent to initiate exfoliation. Varoon *et al.* [39] studied the effect of polystyrene during the pre-expansion process on the formation of highly crystalline nanosheets. α-zirconium phosphate (α-ZrP) was liquid-phase exfoliated using diethylene glycol amine as the exfoliator under ultrasonic assistance by Liu *et al.* [40], and a series of chemicals, including amino alcohols, natural amino acids, alkyl amines and diols, for the direct exfoliation of α-ZrP with the assistance of high-powered ultrasound were studied.

In this study, we present a high-yield exfoliation strategy to redisperse calcined zeolite nanocrystals *via* synergistic use of a tip ultrasonic treatment using 3-aminopropanol as an exfoliating agent and a freeze-drying approach. The high-power ultrasound enables effective exfoliation and high nanoparticle yield by generating sufficient local pressure changes and cavitation effects. During the drying stage, freeze-drying minimizes zeolite sintering after calcination, thereby reducing agglomerate size. In the exfoliation phase, the addition of 3-aminopropanol as an exfoliating agent facilitates the production of nanozeolite with a preserved particle size and high crystallinity. The exfoliation of S-1 zeolite nanoparticles is characterized by XRD, SEM and DLS analyses. The effects of drying methods of as-synthesized zeolite nanoparticle suspension, zeolite contents in frozen nanocrystal suspension, exfoliating agent concentrations, and zeolite doses in ultrasonic suspension on exfoliation efficiency are investigated in detail. A potential mechanism for the exfoliation process was also proposed. By using the above exfoliation strategy, MFI zeolite nanoparticles with an average particle size of ~70 nm, excellent crystallinity, and high yield can be obtained. This approach offers a rapid dispersion method for zeolite nanocrystals, expanding their potential applications in MMMs, adsorption, and catalysis.

2. Experimental

2.1. Chemicals and materials

Sodium hydroxide (NaOH, ≥96%), tetrapropylammonium hydroxide solution (TPAOH, 25% (mass)) and L-lysine (BR) were purchased from Sinopharm chemical Reagent Company. Tetraethyl orthosilicate (TEOS, 98% (mass), Thermo Fisher Scientific), and 3-aminopropanol (≥99%, Aladdin) were used without further purification.

2.2. Synthesis and exfoliation of Silicalite-1 zeolite

Synthesis of S-1 zeolite [27]: Typically, TPAOH was mixed with deionized water and TEOS at room temperature with fast stirring for 2 h, followed by the addition of L-lysine. The gel mixture was continuously stirred in a water bath to evaporate the excess water for a desired water ratio and then transferred into a Teflon-lined stainless-steel autoclave for crystallization. The molar composition of the final synthesis gel was set to 1.0 TEOS/0.45 TPAOH/0.1 L-lysine/9.0 H_2O. The mixture was crystallized at 70 °C for 2 d and 170 °C for 1 d. The product was centrifuged, washed with water several times. And then the cleaned sample was dried by two different methods: oven drying (OD) at 60 °C for 12 h; vacuum freeze drying (VFD) at −50 °C and vacuum pressure of 25 Pa for 48 h. The dried samples were calcinated at 550 °C for 6 h to remove the OSDA. The calcined samples were assigned as C-OD and C-VFD, respectively.

The exfoliation process of S-1 zeolite in water: The as-made 0.5 g C-OD or C-VFD samples were dispersed in 300 ml of water and subjected to 1000 W tip sonication treatment for 4 h, respectively. During the ultrasonic process, the suspension was immersed in an ice-water mixture to prevent the suspension from heating up. The ultrasonic pulse was applied in intervals, being turned on for 4 s and then off for 4 s. The treated sample was then centrifuged at 7800 $r \cdot min^{-1}$ for 30 min to separate the undispersed zeolite crystals, which settled at the bottom. The undispersed zeolite particles were redispersed and centrifuged at 7800 $r \cdot min^{-1}$ for 30 min three times to separate the nanoparticles completely. The supernatants were subsequently centrifuged at 12000 $r \cdot min^{-1}$ for

60 min to collect the nanoparticles. The obtained nanoparticle samples dried under two conditions are denoted as W-OD and W-VFD, where W indicates exfoliation in water, OD and VFD represents two different drying methods.

The exfoliation process of S-1 zeolite in 3-aminopropanol aqueous solution: The C-VFD samples were dispersed in 300 mL of 3-aminopropanol aqueous solution and subjected to 1000 W tip sonication treatment for 30–150 min. To keep the suspension from heating up, the suspension was immersed in an ice-water mixture during the ultrasonic process. The ultrasonic pulse was applied in intervals, being turned on for 4 s and then off for 4 s. The treated sample was then centrifuged at 7800 $r \cdot min^{-1}$ for 30 min to separate the undispersed zeolite particles, which settled at the bottom. The supernatant was subsequently centrifuged at 12000 $r \cdot min^{-1}$ for 60 min to collect the nanoparticles at the bottom. After centrifugation at 12000 $r \cdot min^{-1}$, the resulting supernatant was used to further exfoliate the undispersed zeolite particles. The re-exfoliation of undispersed zeolite particles was repeated to enhance the nanoparticle yield. Afterwards, the collected dispersible nanoparticles were washed three times until neutral. The obtained nanoparticle sample was assigned as A-VFD, where A refers to exfoliation in 3-aminopropanol aqueous solution.

The concentration of the final exfoliated nano zeolite suspension was determined by drying a certain amount of the exfoliated nano zeolite suspension (*e.g.*, 1.0 g) and weighing the dried sample, then the total mass of exfoliated nano zeolite can be obtained. The yield of nano zeolite (%) was calculated as:

$$\text{Nano zeolite yield} = \frac{m_{enz}}{m_{rz}} \quad (1)$$

The amount of unexfoliated zeolite sample can be calculated using the similar way to the total mass amount of exfoliated nano zeolite (m_{enz}). m_{rz} stands for mass of raw zeolite used for exfoliation and m_{us} represents mass of unexfoliated sample. And the recovery rate (%) is calculated as:

$$\text{Recovery rate} = \frac{m_{enz} + m_{us}}{m_{rz}} \quad (2)$$

2.3. Characterizations

The morphology and size of the zeolite samples were observed by scanning electron microscopy (SEM) on a Hitachi SU-8010 equipment. The crystalline phases of the S-1 zeolite were determined using powder X-ray diffraction (XRD) with a Cu Kα radiation source operating at 30 kV and 30 mA, from 5° to 50° with a 0.02° scanning step at 2.5 (°)·min^{-1}. The size distribution of S-1 zeolite nanoparticles suspension was measured by Malvern Zetasizer Nano-ZS equipment. Nitrogen adsorption/desorption measurements were carried out on an AUTOSORB-IQ2-MP analyzer (Quantachrome, USA) at −196 °C after the samples were degassed at 300 °C under vacuum. Raman spectra were recorded on a Renishaw inVia-Reflex confocal Raman microscope with a spectral resolution of 2 cm^{-1} with a laser line at 532 nm. Infrared (IR) spectra of the samples were measured on a Bruker Tensor 27 FT-IR spectrometer.

3. Results and Discussions

3.1. Effect of drying method of S-1 zeolite

The different drying conditions significantly affect the sintering degree of S-1 zeolite after calcination, which in turn influences the difficulty of subsequent exfoliation of nano-zeolite particles. Therefore, we first investigated the impact of drying conditions on the ultrasonic-assisted exfoliation and dispersion of zeolite nanoparticles in water. The SEM image of the synthesized S-1 zeolite is presented in Fig. S1 (Supplementary Material), where spherical particles with a uniform size distribution and an average particle size of 73.5 nm (Table 1) are shown. SEM images of nanosized zeolites after oven-drying-calcination and freeze-drying-calcination, as well as after exfoliation and dispersion in water, are displayed in Fig. 1. By comparing the SEM images of the synthesized nanosized zeolite (Fig. S1), C-OD (Fig. 1(a)) and C-VFD (Fig. 1(b)) samples, it is evident that all calcined samples exhibit varying degrees of agglomeration. The C-OD sample shows a high degree of agglomeration, with numerous nanosized zeolites forming irregular block-like aggregates, while the C-VFD sample exhibits lower agglomeration, with some particles aggregating into a flaky morphology.

Although Fig. 1(c) and (d) do not reveal significant differences in the particle size of the oven-dried-calcined (C-OD) and freeze-dried-calcined (C-VFD) samples after ultrasonic dispersion in water, the average particle sizes measured by DLS (Table 1) and the DLS size distribution (Fig. S2) indicate notable differences. Specifically, the average particle sizes of the W-OD and W-VFD samples after exfoliation in water are 99.8 nm and 76.2 nm, respectively, compared to 73.5 nm for the synthesized nanosized zeolite. The W-OD sample exhibits greater aggregation after exfoliation in water, while the W-VFD sample maintains a particle size close to that of the as-synthesized material, indicating less agglomeration. Photos of C-OD and C-VFD S-1 zeolite particles are shown in Fig. 2, where the volume differences between the two calcined samples are visually illustrated. For the same mass, the C-VFD sample has a significantly larger volume than the C-OD sample, suggesting that the C-VFD sample is looser. This observation is consistent with the SEM results showing the agglomeration state. The yields of zeolite nanoparticles obtained from ultrasonic exfoliation of W-OD and W-VFD were 39% and 52%, respectively, further demonstrating that freeze-dried-calcined samples are more conducive to ultrasonic dispersion in water.

The main factors influencing the agglomeration of zeolite nanoparticles are the drying and calcination processes. In the C-OD sample, the S-1 nanoparticles collected by centrifugation had extremely low water content, leading to a significant reduction in the void between zeolite crystals. Further drying at 60 °C caused the crystals to tightly bind together, resulting in severe agglomeration after calcination. In contrast, the S-1 nanoparticles in the C-VFD sample were initially dispersed in a large volume of water to form a colloidal suspension. After rapid freezing with liquid nitrogen, the particles were freeze-dried at −50 °C *via* ice sublimation diffusion. Ice acts as a solid-phase spacer during freeze-drying, increasing the distance between particles and reducing structural damage to the zeolite nanoparticles. Agglomeration typically occurs when zeolite is treated at high temperatures. Specifically, during calcination at 550 °C, surface atoms or molecules of adjacent inorganic particles diffuse and coalesce, forming sintering necks. This sintering process increases the contact area between particles and reduces porosity, which can negatively impact both the chemical durability and dispersibility of the material [41,42]. The

Table 1
Size and yield of S-1 zeolite after ultrasonic-assisted exfoliation in water.

Sample	Particle size[②]/nm	Nano zeolite yield/%
As-synthesized zeolite	73.5	–
W-OD	99.8	39
W-VFD[①]	76.2	52

[①] Zeolite content in frozen crystals suspension: 4.8 g·L^{-1}.
[②] Z-average size.

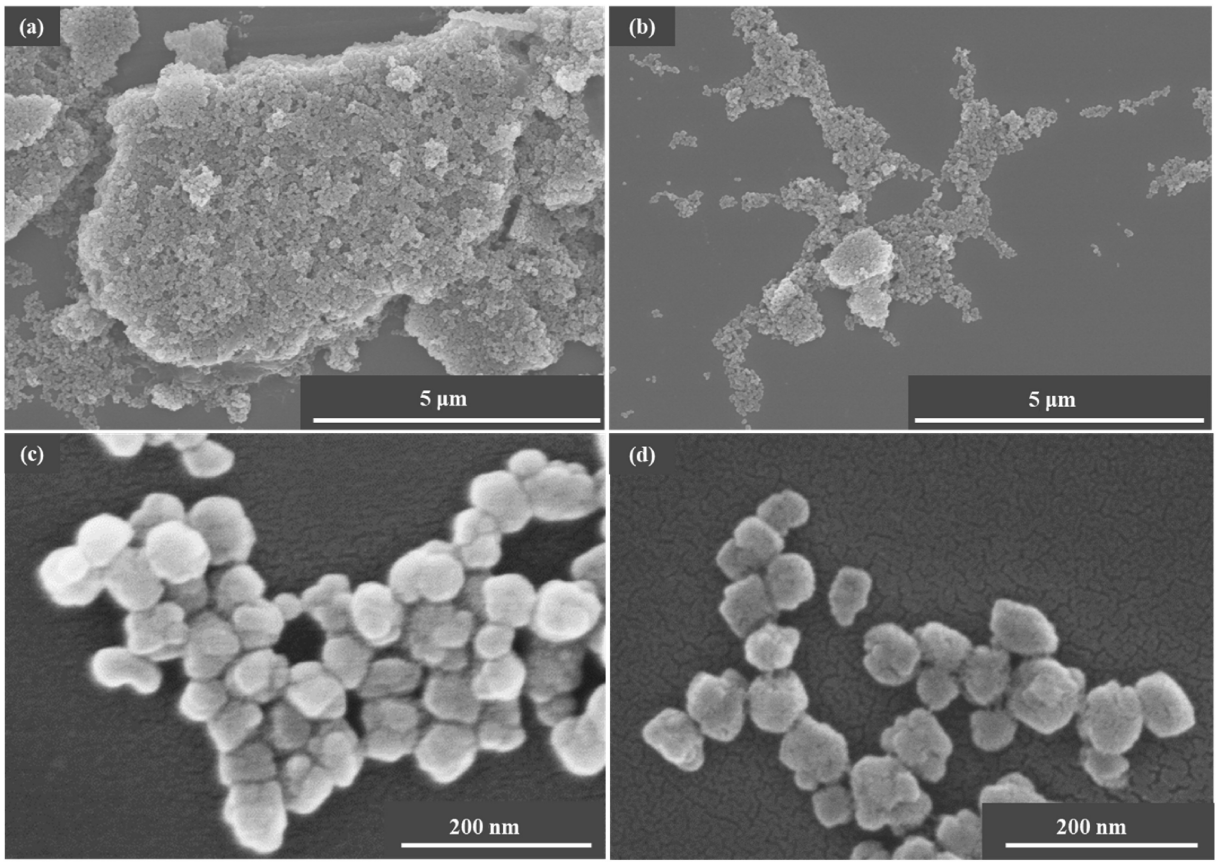

Fig. 1. SEM images of S-1 zeolites: (a) C-OD, (b) C-VFD, (c) W-OD, (d) W-VFD.

nanoparticles from the freeze-drying process remained loose, and the C-VFD sample obtained after calcination preserved a relatively loose structure. This looseness further facilitated the exfoliation process in water by reducing agglomeration, which explains why the yield of zeolite nanoparticles from W-VFD was higher than that from W-OD. The nitrogen adsorption/desorption isotherms for the C-OD and C-VFD samples are presented in Fig. 3, both of which exhibit type I isotherms, characteristic of microporous materials. A distinct hysteresis loop is observed in the high-pressure range (0.9–1.0), attributed to the intercrystalline mesopores formed by the aggregation of nanosized zeolites [43]. The specific surface area and pore volume values are provided in Table S1. Compared to C-OD, the C-VFD sample exhibits a higher BET specific surface area (525 $m^2 \cdot g^{-1}$), micropore surface area (384 $m^2 \cdot g^{-1}$) and micropore volume (0.16 $cm^3 \cdot g^{-1}$), indicating superior crystallinity. These results suggest that freeze-drying effectively reduces sintering during calcination, enhances the yield of zeolite nanoparticles during exfoliation, and preserves the integrity of the micropore structure. As a result, freeze-drying was chosen for the subsequent experiments.

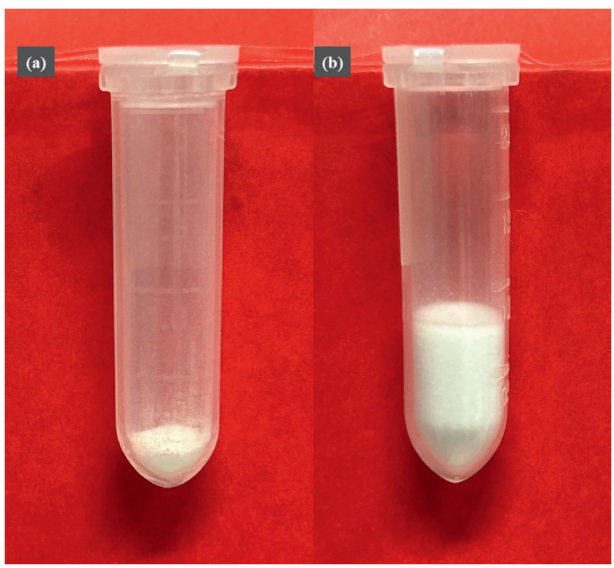

Fig. 2. Optical photos of 0.05 g S-1 zeolite: (a) C-OD, (b) C-VFD.

3.2. Effect of concentration of 3-aminopropanol in ultrasound-assisted exfoliation

As mentioned above, if ultrasound-assisted exfoliation is used only in water, even freeze-dried-calcined samples require 240 min to obtain 52% dispersible zeolite nanocrystals. The exfoliation efficiency is too low to be useful for practical applications. It has been demonstrated that most amino alcohols are able to completely exfoliate α-ZrP with the ultrasound assistance [40]. Therefore, this section examines the impact of adding an exfoliation agent (3-aminopropanol) to ultrasonic dispersion on the nanoparticle dispersion process. Firstly, the pH of the exfoliation system (C-VFD particle content: 1.67 $g \cdot L^{-1}$) was monitored over time in 3-aminopropanol aqueous solutions of varying concentrations, as shown in Fig. 4(a). The pH of the system decreased significantly as

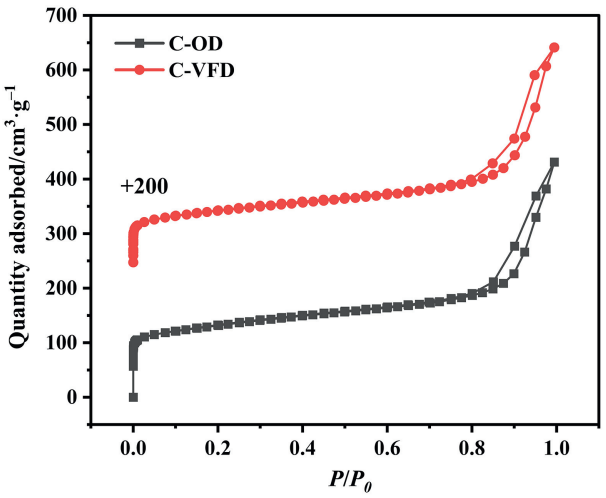

Fig. 3. N_2 sorption isotherms of S-1 zeolites.

the exfoliation time increased, but the time required to reach equilibrium varied. At a 3-aminopropanol concentration of 0.045 mol·L^{-1}, the system stabilized after 80 min. When the concentration was increased to 0.055 mol·L^{-1} or 0.065 mol·L^{-1}, equilibrium was reached in a shorter time, 65 min. However, further increases in concentration did not reduce the time to equilibrium, suggesting that 0.055 mol·L^{-1} is a threshold concentration. Beyond this point, additional exfoliation agent molecules do not effectively interact with more Si–OH groups in the zeolite defects and intercrystalline voids. The reason why the pH value decreases and then reaches equilibrium and the difference in exfoliation time can be attributed to the interaction between the weakly acidic silanol (Si–OH) groups and the weakly basic 3-aminopropanol. This interaction facilitates the insertion of the exfoliation agent into the zeolite structure. Specifically, during the synthesis of MFI zeolite, the basic conditions promote the extraction of tetrahedral silicon atoms from the zeolite lattice, leading to the formation of framework defects. These defects increase the density of silanol groups (Fig. 5), which play a crucial role in the exfoliation process [44–46].

Building on this phenomenon, the amino groups in 3-aminopropanol molecules react with the Si–OH acidic protons present at defect sites and within the intercrystalline voids of the zeolite. This interaction gradually consumes 3-aminopropanol at these acidic sites, leading to a reduction in the pH of suspension. Notably, this acid-base reaction occurs not only on the particle surface but also within the intercrystalline voids, as 3-aminopropanol can penetrate these regions. This dual interaction mechanism facilitates the expansion of intercrystalline voids, highlighting effectiveness of 3-aminopropanol in exfoliating zeolite. The reaction continues until equilibrium is reached, indicating the completion of effective insertion into the zeolite structure. Thus, the pH equilibrium point serves as a key indicator for determining the initial exfoliation time, enabling timely separation of fully exfoliated nanoparticles from residual aggregates. Monitoring pH in this stepwise manner is critical for optimizing dispersion time and maximizing the final yield of zeolite nanoparticles. The cumulative yield and exfoliation time of nanoparticles at different 3-aminopropanol concentrations are shown in Fig. 4(b). After reaching pH equilibrium, centrifugation at 7800 r·min^{-1} revealed that a significant portion of undispersed zeolite particles still settled at the bottom. To enhance the yield of

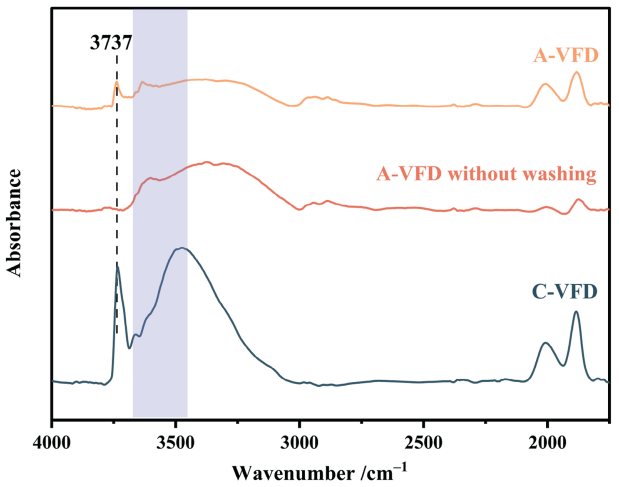

Fig. 5. FTIR spectra of the zeolite samples: C-VFD, A-VFD without washing and A-VFD.

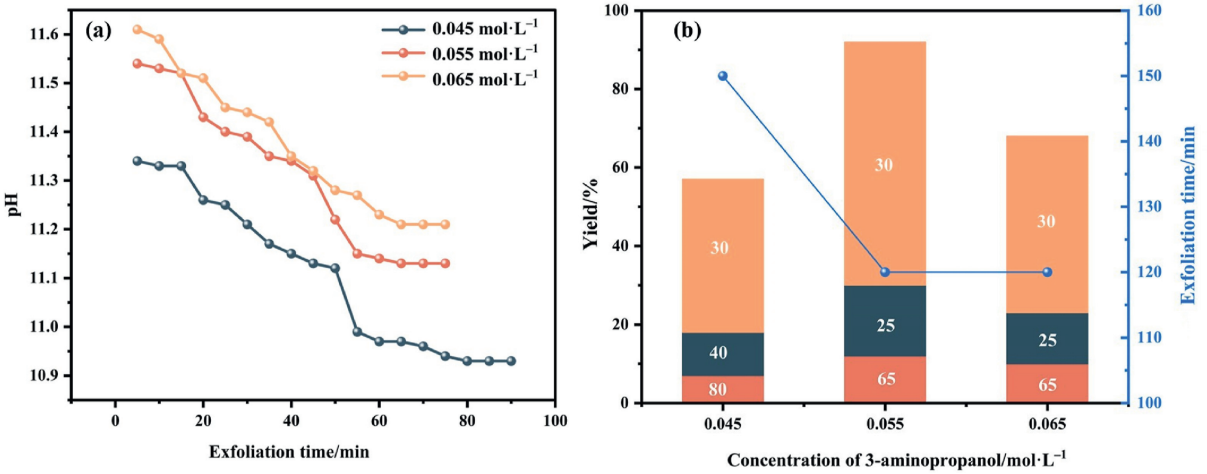

Fig. 4. (a) pH curves of C-VFD zeolite dispersed in 3-aminopropanol aqueous solutions versus exfoliation time and (b) zeolite nanoparticle cumulative yield and exfoliation time of A-VFD zeolites exfoliated in different concentrations of 3-aminopropanol (note: the numbers in column charts indicate the exfoliation time of each individual step in the multiple exfoliation process).

Table 2
Properties of S-1 zeolite nanoparticles exfoliated in different concentrations of 3-aminopropanol.

Sample①	Concentration of 3-aminopropanol solution/mol·L^{-1}	Particle size②/nm	Nano zeolite yield/%	Recovery rate/%	Exfoliation time/min
W-VFD	0	76.2	52	100	240
A-VFD-1	0.045	70.2	57	94	150
A-VFD-2	0.055	69.7	92	96	120
A-VFD-3	0.065	71.4	67	90	120

① Zeolite content in frozen suspension: 4.8 g·L^{-1}, initial exfoliated C-VFD zeolite content: 1.67 g·L^{-1}.
② Z-average size.

fully dispersed nanoparticles, multiple exfoliation cycles were implemented. As shown in Fig. 4(b), the third exfoliation cycle yielded the highest proportion of nanoparticles, indicating that repeated cycles help to further separate nanoparticles from larger aggregates. This improvement can be attributed to two factors: (1) the prior ultrasonic exfoliation reduced particle size, enhancing dispersion, and (2) as nanoparticles were separated, the exposed surface area of agglomerates increased, revealing more reactive Si–OH groups. The results of ultrasonic-assisted exfoliation of C-VFD zeolite into S-1 zeolite nanoparticles, showing different sizes and yields under varying 3-aminopropanol concentrations, are presented in Table 2.

Comparing the particle size distributions from Fig. S2c (W-VFD) and Fig. S3, it is evident that in the absence of 3-aminopropanol, zeolite nanoparticle yield and recovery rates are the lowest, with larger particle sizes (76.2 nm) and a prolonged exfoliation time of 240 min. Introducing 3-aminopropanol at various concentrations significantly improves exfoliation efficiency. At 0.055 mol·L^{-1} (A-VFD-2), the zeolite nanoparticle yield and recovery rate peak at 92% and 96%, respectively, while the exfoliation time is halved to 120 min. This demonstrates that 3-aminopropanol effectively enhances the exfoliation efficiency, with minimal sample loss (4%). However, notable differences emerge at 3-aminopropanol concentrations of 0.045 mol·L^{-1} and 0.065 mol·L^{-1}. In the 0.045 mol·L^{-1} system (A-VFD-1), the lower amino concentration necessitates an extended exfoliation time, but the zeolite nanoparticle yield increases by only 5% compared to the system without an exfoliation agent, while the recovery rate drops by 6%. This suggests that the efficient exfoliation cannot be achieved at this concentration, and prolonged exposure to the alkaline solution reduces recovery. Conversely, at 0.065 mol·L^{-1} (A-VFD-3), the zeolite nanoparticle yield drops by 25% compared to A-VFD-2, with no improvement despite the increased exfoliation agent concentration. The recovery rate also declines to 90%. The decline may result from partial deprotonation of Si–OH groups under high 3-aminopropanol concentrations, forming SiO^-. These groups can form hydrogen bonds with excess 3-aminopropanol, increasing intermolecular forces and promoting particle aggregation, thereby reducing nanoparticle yield. Additionally, the heightened alkalinity may partially dissolve zeolite particles during exfoliation, further lowering recovery rates.

The band at 3737 cm^{-1} in the infrared spectrum corresponds to the free silanol group [47]. A strong band at 3737 cm^{-1} is observed for C-VFD (Fig. 5), indicating the presence of a significant amount of free Si–OH groups. However, after the ultrasonic exfoliation in the 3-aminopropanol solution, the absorption peak in this region for the unwashed A-VFD sample almost completely disappears, suggesting that nearly all the free Si–OH groups have interacted with the weak base of 3-aminopropanol. The band between 3670 cm^{-1} and 3454 cm^{-1} (purple region) is attributed to medium and strong hydrogen-bonded silanol groups within the porous matrix [47], the intensity of the absorption peak at the corresponding position for C-VFD is significantly higher than that of A-VFD and the unwashed A-VFD after exfoliation, indicating that some Si–OH groups in the porous matrix interacted with the amino group. Additionally, the peaks at 3737 cm^{-1} and 3670–3454 cm^{-1} in the infrared spectrum of the washed A-VFD sample are smaller than those in the C-VFD sample. Therefore, the infrared characterization results suggest that 3-aminopropanol interacts with the zeolite nanoparticles, and it is difficult to completely remove the 3-aminopropanol from the nanoparticles through simple water washing. To fully remove 3-aminopropanol from the zeolite nanoparticles, new washing strategies will need to be explored in future studies.

The silanol groups were characterized by Raman spectroscopy (Fig. 6), where the band at 980 cm^{-1} was assigned to the Si–O stretching vibration of the Si–OH group [25,48]. The results are consistent with those observed in the infrared spectrum,

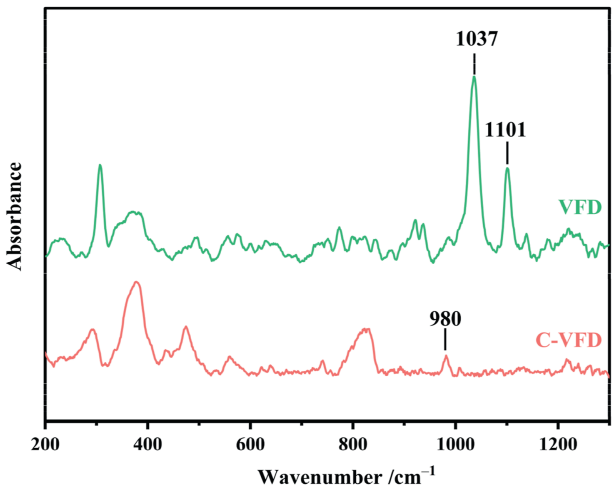

Fig. 6. Raman spectra of the zeolite samples: VFD and C-VFD.

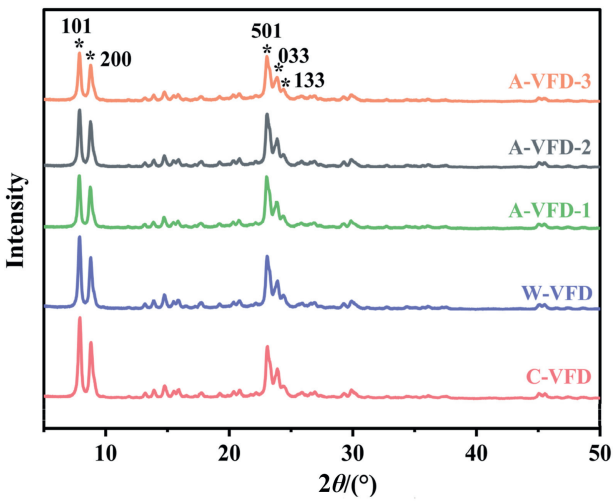

Fig. 7. XRD patterns of exfoliated and unexfoliated S-1 zeolite.

confirming that C-VFD contains silanol sites that react with 3-aminopropanol. Raman spectroscopy of the VFD sample shows prominent peaks corresponding to TPAOH molecules, specifically in the range of 1030–1150 cm^{-1}, which can be attributed to the C–N stretching vibration mode [49].

XRD patterns of all samples align with the characteristic peaks of MFI zeolite (Fig. 7). Compared to the C-VFD sample, the diffraction peak intensity of the W-VFD sample remains virtually unchanged, indicating that the ultrasonic exfoliation process in water does not significantly alter the zeolite lattice structure. However, when the 3-aminopropanol concentration reaches 0.065 $mol \cdot L^{-1}$, the intensity of the diffraction peaks corresponding to the (101) and (200) crystal planes in the A-VFD sample significantly decreases, suggesting that the exfoliation process may involve etching, which alters the intensity of the diffraction peaks and reduces crystallinity of the particles.

Furthermore, TEM images of the exfoliated zeolite nanoparticles (Fig. 8) show no significant change in size or morphology compared to the as-synthesized zeolite (Fig. S1), indicating that the exfoliation process does not notably affect the overall particle structure. Additionally, TEM images (Fig. 8(b)–(d), and (f)) reveal the presence of mesopores in the exfoliated nanoparticles, likely resulting from etching by 3-aminopropanol during the exfoliation process. As a representative, the texture properties of A-VFD-2 sample were measured by nitrogen adsorption experiment. As shown in Fig. 9, A-VFD-2 exhibits a type I adsorption-desorption isotherm, typical of microporous materials, along with a hysteresis loop characteristic of mesoporous materials. This hysteresis loop is attributed to capillary condensation, which is commonly observed in mesoporous materials [43]. Compared to the C-VFD sample, the BET specific surface area (541 $m^2 \cdot g^{-1}$), micropore surface area (388 $m^2 \cdot g^{-1}$), and micropore volume (0.17 $cm^3 \cdot g^{-1}$) of A-VFD-2 show only slight differences (Table S1), indicating that the crystallinity of the material is well preserved after the exfoliation process. In summary, the optimal 3-aminopropanol concentration for the exfoliation suspension was determined to be 0.055 $mol \cdot L^{-1}$.

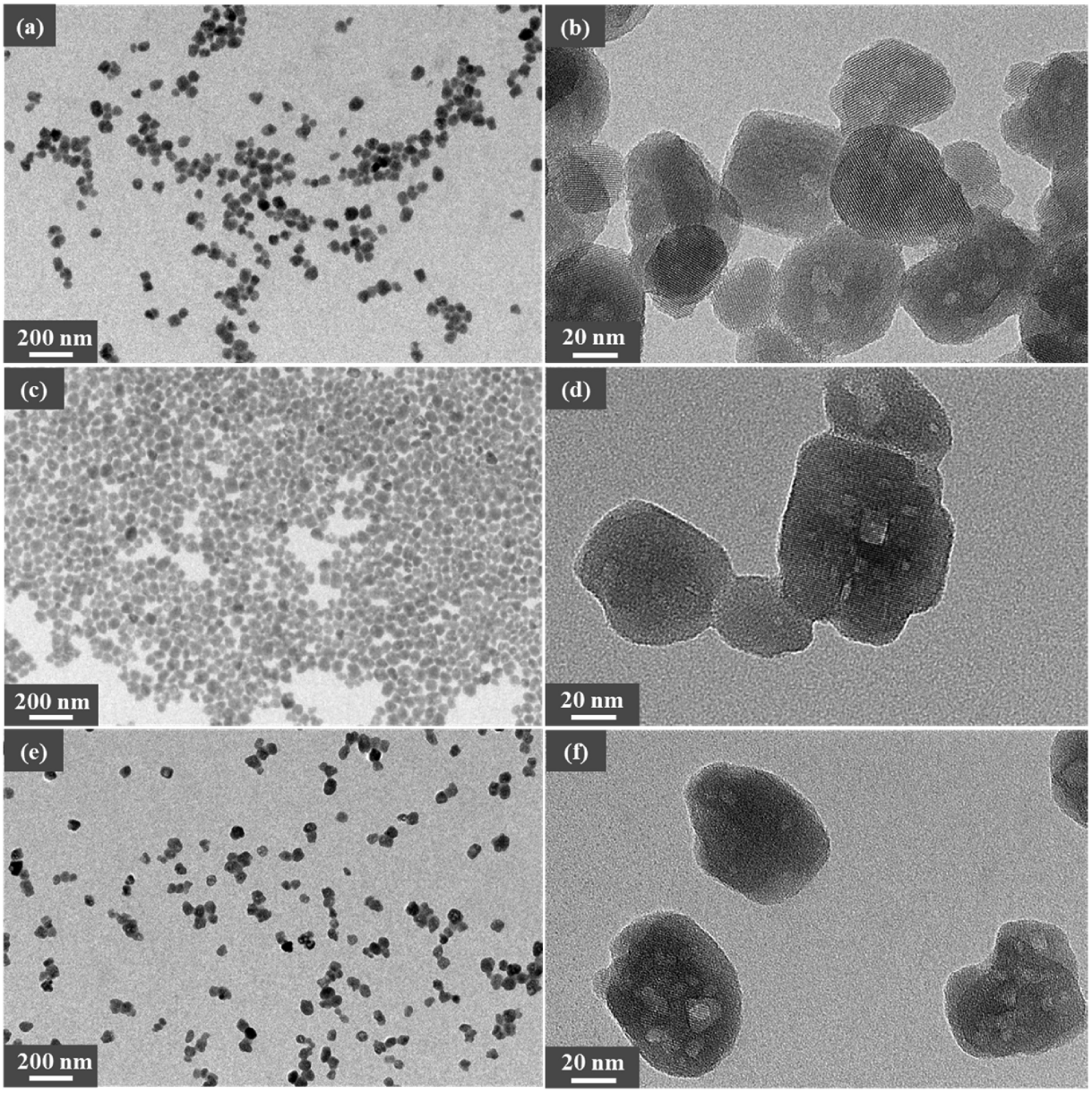

Fig. 8. TEM images of zeolite nanoparticles: (a, b) A-VFD-1, (c, d) A-VFD-2, (e, f) A-VFD-3.

This concentration strikes a balance between the high exfoliation efficiency and minimization of over-exfoliation, ensuring effective exfoliation while maintaining a high yield and recovery rate of zeolite nanoparticles.

3.3. Effect of zeolite content in frozen suspension

After determining the optimal 3-aminopropanol concentration of 0.055 mol·L^{-1} for exfoliation, we investigated the effect of the content of synthetic zeolite in the frozen suspension. The zeolite content determines the ice content during freeze-drying, which indirectly affects the exfoliation efficiency [50,51]. Ultrasound-assisted exfoliation of C-VFD zeolites with varying zeolite contents in the frozen suspension resulted in A-VFD nanoparticles with different sizes and yields, as shown in Table 3. As the zeolite content increased from 4.8 g·L^{-1} to 28.8 g·L^{-1}, the yield of exfoliated nanoparticles continuously decreased, dropping significantly from 92% to 57%, while the recovery rate also showed a slight decrease. When the zeolite content in the frozen suspension increased from 4.8 g·L^{-1} to 14.4 g·L^{-1}, the particle size of the exfoliated nanoparticles remained relatively stable, increasing from 69.7 nm to 71.9 nm. However, at a zeolite content of 28.8 g·L^{-1}, the particle size increased to 80.5 nm (Fig. S4). The SEM images of the calcinated samples with different zeolite contents in the frozen suspensions are shown in Fig. 10.

The order of agglomeration volume is $V_{C\text{-}VFD\text{-}6} > V_{C\text{-}VFD\text{-}5} > V_{C\text{-}VFD\text{-}4} > V_{C\text{-}VFD\text{-}2}$, which correlates with the yield, suggesting a negative relationship between agglomeration and yield. It is inferred that the decrease of the nanoparticle yield with increasing the zeolite content is linked to the significant agglomeration, which occurs under high concentration conditions during calcination. Notably, both the C-VFD-6 sample (Fig. 10(g)) and the C-OD sample (Fig. 1(a)) exhibit larger agglomeration volumes, and the particle sizes of the exfoliated nanoparticles exceed that of the as-synthesized zeolite. This indicates that, although freeze-drying helps reduce sintering and improves the exfoliation efficiency, an excessively high zeolite content in the frozen suspension can negate these advantages and negatively affect subsequent exfoliation results. The underlying reason is likely that the zeolite content in the frozen suspension indirectly impacts the freeze-drying process by altering the ice content in the material. Zeolite particles are first rapidly frozen in liquid nitrogen at −196 °C, then undergo freeze-drying to remove the ice *via* sublimation. This rapid freezing prevents zeolite particles migration due to diffusion limitations, resulting in a highly uniform zeolite particle distribution. The strict control of frozen zeolite content during freezing plays a crucial role in the formation of ice crystals. As the ice crystals sublimate during freeze-drying, this effectively eliminates the capillary migration that typically occurs during the evaporation process in conventional oven drying methods. Capillary migration can lead to particle agglomeration and the collapse of pore structures due to localized pressure gradients and water transport within the sample. By avoiding this, freeze-drying reduces the agglomeration of zeolite nanoparticles and further helps preserve the pore structure of zeolite nanoparticles [50,51]. This is reflected in the higher micropore specific surface area, as shown in Table S1, the micropore specific surface area of the C-VFD sample is 50 m^2·g^{-1} larger than that of the C-OD sample. As the zeolite content increases in the frozen suspension, the volume of the ice crystals decreases, limiting the effective dispersion of the zeolite nanoparticles. This results in the formation of larger zeolite agglomerates after calcination, characterized by irregular shapes and partial bending.

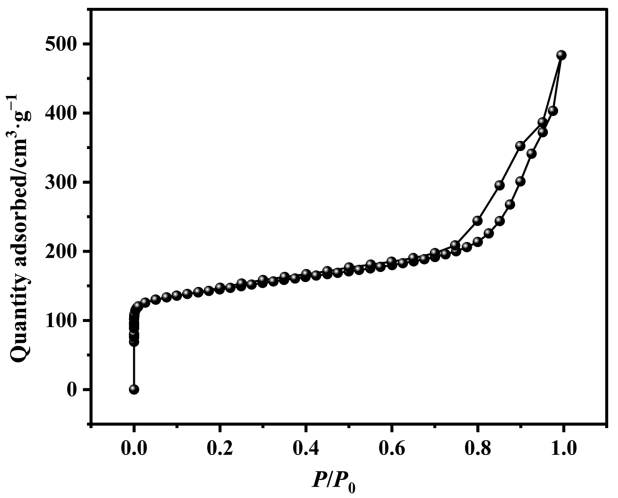

Fig. 9. N_2 sorption isotherms of A-VFD-2 sample.

The increased size and density of these agglomerates hinder the ability of the exfoliating agent, 3-aminopropanol, to effectively penetrate the zeolite crystals and expand the intercrystalline voids. The cumulative yields of exfoliated nanoparticles under different zeolite contents in the frozen suspensions (Fig. 11) further support this conclusion. For the A-VFD-5 sample, an additional 30 min of exfoliation time was applied; however, its nanoparticle yield remained significantly lower than that of A-VFD-2 and A-VFD-4. Similarly, the initial pH stabilization phase for the A-VFD-6 sample was extended by 25 min compared to the other samples. Despite having the same total exfoliation time as A-VFD-5, the nanoparticle yield of A-VFD-6 was even lower. The total yield and recovery rates for A-VFD-5 and A-VFD-6, both with higher zeolite contents in frozen suspensions, were notably lower than those of A-VFD-2 and A-VFD-4. These results indicate that the reduced exfoliation efficiency caused by the high zeolite content in the frozen suspension cannot be compensated simply by extending the exfoliation time. Based on these findings, a zeolite content of 4.8 g·L^{-1} in the frozen suspension was identified as optimal, ensuring the maximum yield with minimal particle agglomeration.

Table 3
Effects of S-1 zeolite content in frozen suspension on properties of nanoparticles.

Sample①	Frozen zeolite content②/g·L^{-1}	Particle size③/nm	Nano zeolite yield/%	Recovery rate/%	Exfoliation time/min
A-VFD-2	4.8	69.7	92	96	120
A-VFD-4	9.6	71.5	80	95	120
A-VFD-5	14.4	71.9	64	92	150
A-VFD-6	28.8	80.5	57	92	150

① Concentration of 3-aminopropanol solution: 0.055 mol·L^{-1}, initial C-VFD zeolite content in exfoliated suspension: 1.67 g·L^{-1}.
② In frozen suspension.
③ Z-average size.

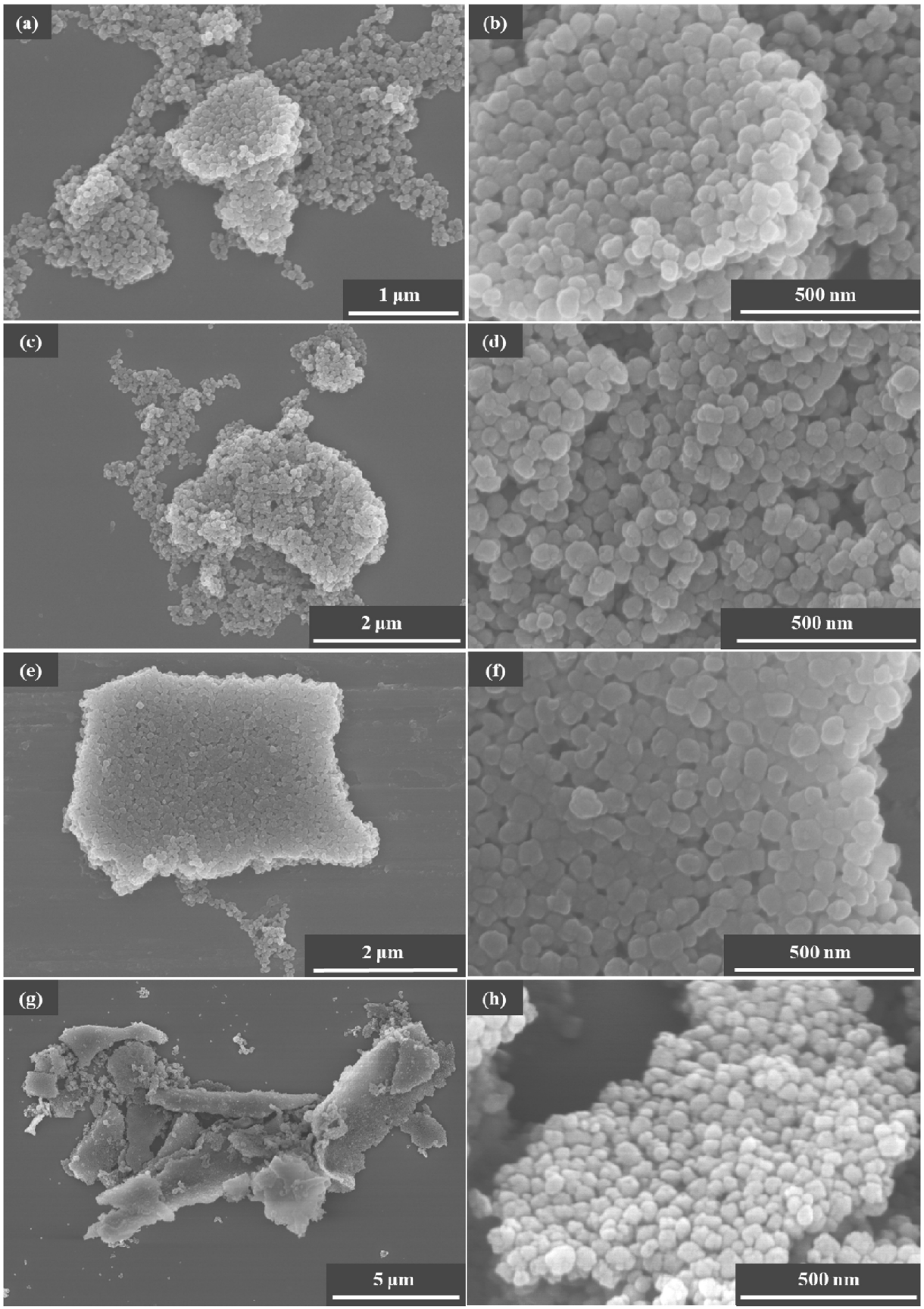

Fig. 10. SEM images of C-VFD zeolites with different zeolite contents in frozen suspension: (a, b) 4.8 g·L^{-1}, (c, d) 9.6 g·L^{-1}, (e, f) 14.4 g·L^{-1}, (g, h) 28.8 g·L^{-1}.

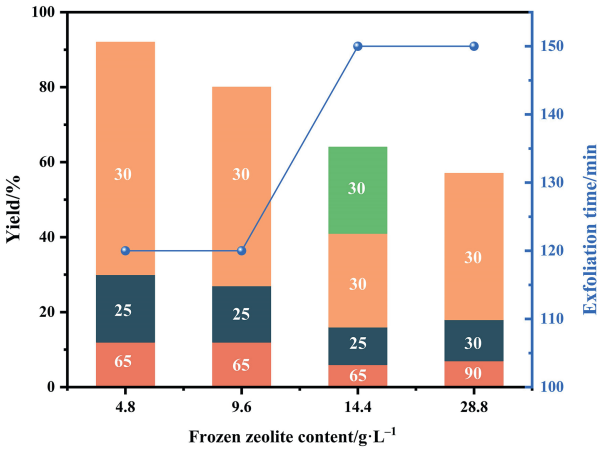

Fig. 11. Effect of zeolite content in frozen suspension on yield of A-VFD zeolite (the numbers in column charts indicate the exfoliation time of each individual step in the multiple exfoliation process).

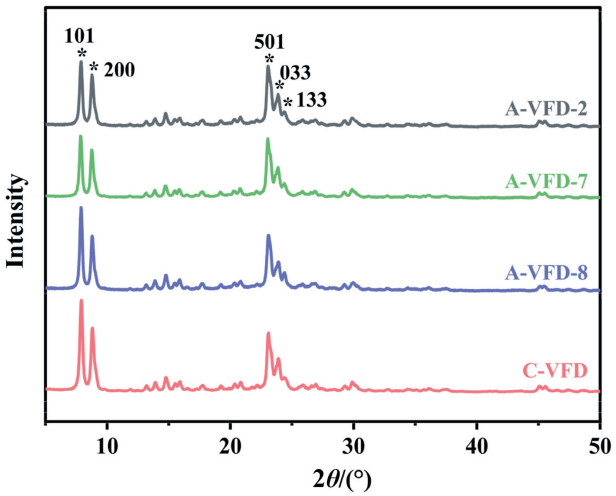

Fig. 12. XRD patterns of exfoliated and unexfoliated S-1 zeolites.

3.4. Effect of zeolite content in ultrasonic-assisted exfoliation suspension

To enhance the exfoliation efficiency, the influence of zeolite content in the exfoliation suspension was systematically investigated, and the effect of the ultrasonic output power on the structural integrity and yield of the exfoliated zeolite nanoparticles was explored. The results are presented in Table 4. As the zeolite content in the exfoliation suspension decreased, from 1.67 g·L^{-1} (A-VFD-2) to 0.33 g·L^{-1} (A-VFD-8), the yield and recovery rate of the A-VFD zeolite nanoparticles varied by approximately 3%. However, the required exfoliation time was dramatically reduced from 120 min to 30 min, significantly improving the exfoliation efficiency. The XRD patterns of the samples are shown in Fig. 12. The diffraction peak intensity of A-VFD-8 is very close to that of C-VFD, while the intensities of A-VFD-7 and A-VFD-2 are lower. This suggests that the shortened ultrasound-assisted exfoliation time helps mitigate lattice damage in the zeolite structure. The ultrasonic intensity is related to the cavitation potential, which enhances zeolite exfoliation and dispersion by increasing shear forces [52].

However, an excessive ultrasonic intensity can introduce lattice defects in the zeolite structure, necessitating careful optimization to balance the effective exfoliation with the structural integrity. In a 0.055 mol·L^{-1} 3-aminopropanol aqueous solution, the pH changes of the system with different zeolite concentrations in the exfoliation suspensions are shown in Fig. 13a. The pH equilibrium time for the A-VFD-8 sample was only 30 min, just 25% of the ultrasonic treatment time required for A-VFD-2. Moreover, only one exfoliation step was needed to achieve a 95% yield of zeolite nanoparticles (Fig. 13b). This high efficiency is attributed to the increased relative output power of the ultrasound and the enhanced contact between the C-VFD-8 sample, the exfoliation agent and water. This interaction allows a larger proportion of active Si—OH sites to participate in the reaction, accelerating the nanoparticle exfoliation and dispersion. As the zeolite concentration in the exfoliation suspension increases, the time required to reach pH equilibrium also increases, and the number of exfoliation cycles triples. These findings highlight the importance of selecting an optimal zeolite content in the ultrasonic suspension based on the ultrasound output power. For a 1000 W tip sonication, using 0.33 g·L^{-1} as the zeolite content in the exfoliation suspension is ideal for achieving the best balance between crystal integrity, yield, and recovery efficiency.

3.5. Exfoliation mechanism

As shown in Fig. 14, in the first step, the insertion of exfoliant molecules is facilitated by an acid-base reaction between the amino groups of 3-aminopropanol and the Si—OH groups located at the structural defects and surfaces of the zeolite. This reaction leads to the embedding of the exfoliant molecules into the intergranular spaces or crystal defects of the zeolite, gradually increasing the intergranular voids. The second step involves water-induced expansion. The enlarged intergranular spacing allows water molecules to penetrate these spaces, causing the zeolite structure to swell until it is completely exfoliated. The hydrophilic functional groups of 3-aminopropanol enhance water entry, further promoting the exfoliation process [40]. Ultrasonic cavitation plays a crucial auxiliary role in both stages of the exfoliation process. Cavitation is induced by high-power ultrasound and involves the formation, growth, and collapse of microbubbles in a liquid medium. This cyclical process generates intense local energy. When these bubbles collapse, they create strong shear forces and localized heating, temporarily increasing the temperature and pressure around the zeolite particles. This cavitation effect accelerates the insertion of exfoliant molecules by increasing molecular motion and reducing intermolecular cohesion within the zeolite. Specifically, cavitation enhances the acid-base reaction between the amino groups and Si—OH groups, promoting faster and more extensive insertion of the exfoliant. Additionally, the continuous cycle of bubble growth

Table 4
Effect of C-VFD zeolite content in exfoliated suspension on properties of A-VFD zeolite nanoparticles.

Sample[①]	Exfoliated zeolite content/g·L^{-1}	Particle size[②]/nm	Nano zeolite yield/%	Recovery rate/%	Exfoliation time/min
A-VFD-2	1.67	69.7	92	96	120
A-VFD-7	1.00	69.9	95	97	95
A-VFD-8	0.33	68.7	95	99	30

① Concentration of 3-aminopropanol solution: 0.055 mol·L^{-1}, zeolite content in frozen suspension: 4.8 g·L^{-1}.
② Z-average size.

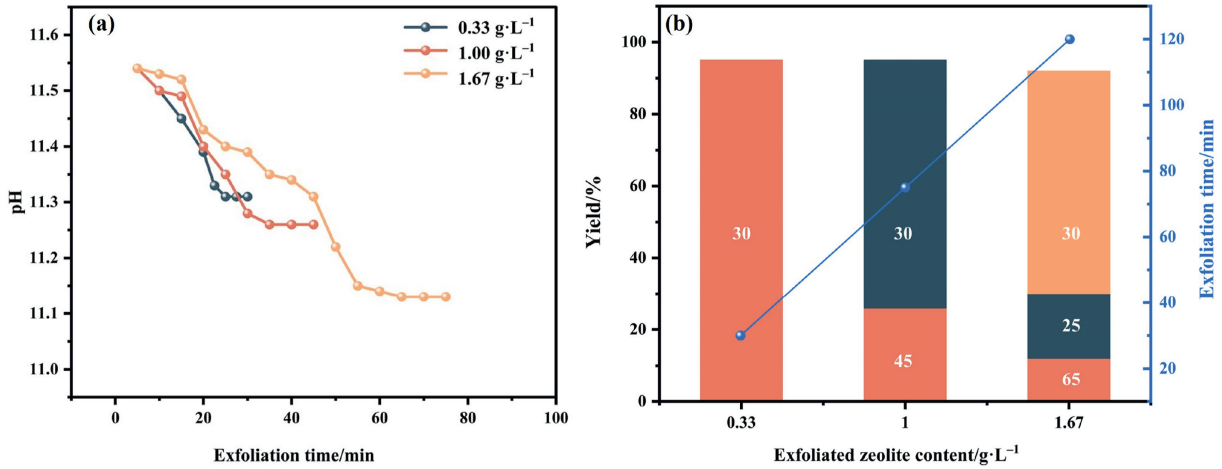

Fig. 13. (a) pH curves of the exfoliated C-VFD zeolite suspension and (b) Effect of exfoliated zeolite content in exfoliated suspension on yield of A-VFD zeolite (Note: the numbers in column charts indicate the exfoliation time of each individual step in the multiple exfoliation process).

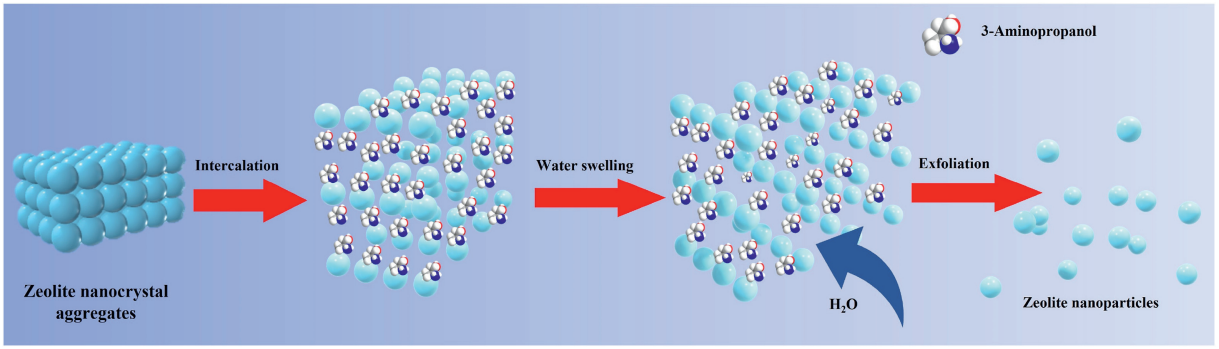

Fig. 14. Schematic representation of ultrasonic-assisted exfoliation in 3-aminopropanol aqueous solution.

and collapse helps evenly disperse the exfoliant molecules, improving the overall stability of the system and allowing it to reach equilibrium in a shorter time.

4. Conclusions

In summary, this study successfully achieved the dispersion of MFI zeolite nanoparticles by removing the OSDA through a method that combines freeze-drying, calcination, and ultrasound cell disruptor. The process begins by quickly freezing a 4.8 $g \cdot L^{-1}$ S-1 zeolite suspension using liquid nitrogen, followed by freeze-drying to form ice crystals, which help maintain a loose structure. The zeolite is then calcinated, and 0.055 $mol \cdot L^{-1}$ 3-aminopropanol is used as an exfoliation agent to facilitate a rapid ultrasonic-assisted exfoliation of a 0.33 $g \cdot L^{-1}$ S-1 zeolite suspension. Within 30 min, zeolite nanoparticles with good crystallinity and an average particle size of approximately 70 nm are obtained, with a yield as high as 95%. This method effectively addresses the issue of particle agglomeration after calcination. By analyzing the key factors influencing the exfoliation process, a primary exfoliation mechanism was proposed, which involves the insertion of exfoliation molecules followed by the expansion of water molecules inserted into the zeolite. Both steps are significantly accelerated by ultrasonic cavitation. 3-Aminopropanol serves as an efficient exfoliation agent due to its dual functionality: the alkalinity of the amino group and the hydrophilicity of the hydroxyl group. This dual action enhances the exfoliation efficiency while preserving crystallinity, achieving high yield, and maintaining a high recovery rate of zeolite nanoparticles. This study presents a promising method for the rapid dispersion of sintered MFI zeolite nanoparticle agglomerates, which has potential for expanding applications in various fields.

CRediT Authorship Contribution Statement

Xinyi Gao: Writing – original draft, Methodology, Investigation, Conceptualization. Qiancheng Zheng: Methodology. Zhengbao Wang: Writing – review & editing, Supervision, Project administration, Funding acquisition.

Declaration of Competing Interest

The authors declare that they have no known competing financial interests or personal relationships that could have appeared to influence the work reported in this paper.

Acknowledgements

This work is supported by the Natural Science Foundation of Zhejiang Province, China (LD24B060002), National Key Research and Development Program of China (2021YFB3801102) and the Fundamental Research Funds for the Central Universities (226-2024-00060).

Supplementary Material

Supplementary data to this article can be found online at https://doi.org/10.1016/j.cjche.2025.02.029.

References

[1] J. Kobler, H. Abrevaya, S. Mintova, T. Bein, High-silica zeolite-β: from stable colloidal suspensions to thin films, *J. Phys. Chem. C* 112 (37) (2008) 14274–14280.

[2] N.V. Kolesnichenko, N.N. Ezhova, O.V. Yashina, Formation of MFI-type zeolite nanoparticles and zeolite-based suspensions, *Petrol. Chem.* 56 (9) (2016) 827–831.

[3] J. Zhou, W. Fan, Y.D. Wang, Z.K. Xie, The essential mass transfer step in hierarchical/nano zeolite: surface diffusion, *Natl. Sci. Rev.* 7 (11) (2019) 1630–1632.

[4] M. Rutkowska, L. Chmielarz, D. Macina, Z. Piwowarska, B. Dudek, A. Adamski, S. Witkowski, Z. Sojka, L. Obalová, C.J. van Oers, P. Cool, Catalytic decomposition and reduction of N_2O over micro-mesoporous materials containing beta zeolite nanoparticles, *Appl. Catal. B Environ.* 146 (2014) 112–122.

[5] L. Tosheva, B. Mihailova, L.H. Wee, B. Gasharova, K. Garbev, A.M. Doyle, In-direct observation of structured incipient zeolite nanoparticles in clear precursor solutions, *Angew. Chem. Int. Ed.* 47 (45) (2008) 8650–8653.

[6] T.M. Davis, T.O. Drews, H. Ramanan, C. He, J.S. Dong, H. Schnablegger, M.A. Katsoulakis, E. Kokkoli, A.V. McCormick, R.L. Penn, M. Tsapatsis, Mechanistic principles of nanoparticle evolution to zeolite crystals, *Nat. Mater.* 5 (2006) 400–408.

[7] P. Guo, J. Shin, A.G. Greenaway, J.G. Min, J. Su, H.J. Choi, L. Liu, P.A. Cox, S.B. Hong, P.A. Wright, X. Zou, A zeolite family with expanding structural complexity and embedded isoreticular structures, *Nature* 524 (7563) (2015) 74–78.

[8] P.Y. Yu, G. Yang, Y.M. Chai, L. Tosheva, C.Z. Wang, H.Q. Jiang, C.G. Liu, H.L. Guo, Self-limiting growth of thin dense LTA membranes boosts H_2 gas separation performance, *Chem. Eng. J.* 479 (2024) 147629.

[9] X.Q. Wang, P.C. Xu, L. Tang, Y. Chen, X.X. Li, Nano beta zeolites catalytic-cracking effect on hydrochlorofluorocarbon molecule for specific detection of Freon, *J. Mater. Chem. A* 9 (27) (2021) 15321–15328.

[10] Y.E. Yan, X. Guo, Y.H. Zhang, Y. Tang, Future of nano-/hierarchical zeolites in catalysis: gaseous phase or liquid phase system, *Catal. Sci. Technol.* 5 (2) (2015) 772–785.

[11] H. Yan, N.K. Ma, Z.Y. Zhan, Z.B. Wang, Fabrication of zeolite NaA membranes on hollow fibers using nano-sized seeds exfoliated from mesoporous zeolite crystals, *Microporous Mesoporous Mater.* 215 (2015) 244–248.

[12] K. Lazarova, H. Awala, S. Thomas, M. Vasileva, S. Mintova, T. Babeva, Vapor responsive one-dimensional photonic crystals from zeolite nanoparticles and metal oxide films for optical sensing, *Sensors* 14 (7) (2014) 12207–12218.

[13] M. Tsotsalas, M. Busby, E. Gianolio, S. Aime, L. De Cola, Functionalized nanocontainers as dual magnetic and optical probes for molecular imaging applications, *Chem. Mater.* 20 (18) (2008) 5888–5893.

[14] J.H. Ye, J.C. Tan, High-performance triboelectric nanogenerators incorporating chlorinated zeolitic imidazolate frameworks with topologically tunable dielectric and surface adhesion properties, *Nano Energy* 114 (2023) 108687.

[15] G. Calzaferri, S. Huber, H. Maas, C. Minkowski, Host-guest antenna materials, *Angew. Chem. Int. Ed.* 42 (32) (2003) 3732–3758.

[16] H.S. Kim, N.C. Jeong, K.B. Yoon, Photovoltaic effects of CdS and PbS quantum dots encapsulated in zeolite Y, *Langmuir* 27 (23) (2011) 14678–14688.

[17] P. Lakhera, V. Chaudhary, S. Singh, N. Vishwakarma, C. Sanchez Huertas, P. Kumar, S. Kumar, Detection of glycosylated hemoglobin on boronic acid-modified zeolitic imidazolate framework-8 nanoparticles, *ACS Appl. Nano Mater.* 6 (24) (2023) 22857–22864.

[18] S. Gutiérrez-Rubio, M. Shamzhy, Č. J, D.P. Serrano, I. Moreno, J.M. Coronado, Vapor phase acylation of guaiacol with acetic acid over micro, nano and hierarchical MFI and BEA zeolites, *Appl. Catal. B Environ.* 285 (2021) 119826.

[19] C.Y. Chuah, J. Lee, Y.P. Bao, J.H. Song, T.H. Bae, High-performance porous carbon-zeolite mixed-matrix membranes for CO_2/N_2 separation, *J. Membr. Sci.* 622 (2021) 119031.

[20] K. Zarshenas, A. Raisi, A. Aroujalian, Mixed matrix membrane of nano-zeolite NaX/poly (ether-*block*-amide) for gas separation applications, *J. Membr. Sci.* 510 (2016) 270–283.

[21] Q.C. Zheng, H.Y. Zhang, H.F. Tan, Z.B. Wang, Rapid and facile synthesis of nanosized silicalite-1 zeolites from solid silica in a semisolid-like system *via* a two-step crystallization method, *Ind. Eng. Chem. Res.* 63 (14) (2024) 6121–6131.

[22] Q.C. Zheng, H.Y. Zhang, J. Li, X.T. Yu, X.Y. Gao, Z.B. Wang, Amino acid assisted-construction of 2D-hierarchical MFI zeolites for adsorption of Rhodamine B, *Sep. Purif. Technol.* 358 (2025) 130414.

[23] H. Konno, T. Tago, Y. Nakasaka, R. Ohnaka, J.I. Nishimura, T. Masuda, Effectiveness of nano-scale ZSM-5 zeolite and its deactivation mechanism on catalytic cracking of representative hydrocarbons of naphtha, *Microporous Mesoporous Mater.* 175 (2013) 25–33.

[24] C.S. Zhang, S.Q. Chu, J. Jiang, J.C. Zhao, S. Wen, B. Sun, W. Xu, Minute-scale synthesis of nano silicalite-1 zeolites, *Front. Chem.* 10 (2022) 860795.

[25] J. Grand, S.N. Talapaneni, A. Vicente, C. Fernandez, E. Dib, H.A. Aleksandrov, G. N. Vayssilov, R. Retoux, P. Boullay, J.P. Gilson, V. Valtchev, S. Mintova, One-pot synthesis of silanol-free nanosized MFI zeolite, *Nat. Mater.* 16 (10) (2017) 1010–1015.

[26] C.S. Zhang, Q.M. Wu, C. Lei, S.C. Han, Q.Y. Zhu, S. Maurer, D. Dai, A.N. Parvulescu, U. Müller, X.J. Meng, F.S. Xiao, An efficient, rapid, and non-centrifugation synthesis of nanosized zeolites by accelerating the nucleation rate, *J. Mater. Chem. A* 6 (42) (2018) 21156–21161.

[27] Q. Zhang, G.R. Chen, Y.Y. Wang, M.Y. Chen, G.Q. Guo, J. Shi, J. Luo, J.H. Yu, High-quality single-crystalline MFI-type nanozeolites: a facile synthetic strategy and MTP catalytic studies, *Chem. Mater.* 30 (8) (2018) 2750–2758.

[28] Y. Guo, T.J. Sun, X.W. Liu, Q.L. Ke, X.L. Wei, Y.M. Gu, S.D. Wang, Cost-effective synthesis of CHA zeolites with controllable morphology and size, *Chem. Eng. J.* 358 (2019) 331–339.

[29] S. Mintova, J.P. Gilson, V. Valtchev, Advances in nanosized zeolites, *Nanoscale* 5 (15) (2013) 6693–6703.

[30] H.T. Wang, Z.B. Wang, Y.S. Yan, Colloidal suspensions of template-removed zeolite nanocrystals, *Chem. Commun.* 23 (2000) 2333–2334.

[31] Y. Li, W.B. Krantz, T.S. Chung, A novel primer to prevent nanoparticle agglomeration in mixed matrix membranes, *AIChE. J.* 53 (9) (2007) 2470–2475.

[32] H. Chen, Y. Zhou, Z. Tošner, Č. Jiří, M. Opanasenko, Synthesis of aggregation-resistant MFI nanoparticles, *Catal. Today* 354 (2020) 151–157.

[33] W.J. Roth, T. Sasaki, K. Wolski, Y.J. Song, D.M. Tang, Y. Ebina, R.Z. Ma, J. Grzybek, K. Kałahurska, B. Gil, M. Mazur, S. Zapotoczny, J. Cejka, Liquid dispersions of zeolite monolayers with high catalytic activity prepared by soft-chemical exfoliation, *Sci. Adv.* 6 (12) (2020) eaay8163.

[34] A. Corma, V. Fornes, S.B. Pergher, T.L.M. Maesen, J.G. Buglass, Delaminated zeolite precursors as selective acidic catalysts, *Nature* 396 (6709) (1998) 353–356.

[35] W.J. Roth, T. Sasaki, K. Wolski, B. Gil, S. Zapotoczny, J. Čejka, M. Kubů, M. Mazur, Y. Ebina, N. Sakai, D.M. Tang, R.Z. Ma, Exfoliating layered zeolite MFI into unilamellar nanosheets in solution as precursors for the synthesis of hierarchical nanocomposites and oriented films, *Inorg. Chem. Front.* 10 (5) (2023) 1511–1521.

[36] P. Loch, D. Schuchardt, G. Algara-Siller, P. Markus, K. Ottermann, S. Rosenfeldt, T. Lunkenbein, W. Schwieger, G. Papastavrou, J. Breu, Nematic suspension of a microporous layered silicate obtained by forceless spontaneous delamination *via* repulsive osmotic swelling for casting high-barrier all-inorganic films, *Sci. Adv.* 8 (20) (2022) eabn9084.

[37] W.J. Roth, T. Sasaki, K. Wolski, Y. Ebina, D.M. Tang, Y. Michiue, N. Sakai, R.Z. Ma, O. Cretu, J. Kikkawa, K. Kimoto, K. Kalahurska, B. Gil, M. Mazur, S. Zapotoczny, J. Čejka, J. Grzybek, A. Kowalczyk, Exfoliated ferrierite-related unilamellar nanosheets in solution and their use for preparation of mixed zeolite hierarchical structures, *J. Am. Chem. Soc.* 143 (29) (2021) 11052–11062.

[38] B. Wang, N.N. Wang, X.W. Li, R.F. Zhou, W.H. Xing, Exfoliation of lamellar SAPO-34 zeolite to nanosheets and synthesis of thin SAPO-34 membranes by a nanosheet-seeded secondary growth approach, *J. Membr. Sci.* 645 (2022) 120177.

[39] K. Varoon Agrawal, X. Zhang, B. Elyassi, D.D. Brewer, M. Gettel, S. Kumar, J.A. Lee, S. Maheshwari, A. Mittal, C.Y. Sung, M. Cococcioni, L.F. Francis, A.V. McCormick, K.A. Mkhoyan, M. Tsapatsis, Dispersible exfoliated zeolite nanosheets and their application as a selective membrane, *Science* 334 (6052) (2011) 72–75.

[40] L. Liu, P.J. Fang, C.H. Yan, J.J. Ma, J.Z. Zhang, J.D. Zhou, H. Sun, X. Ji, C.Z. Xu, Z. W. Tong, Ultrasonic-assisted rapid and highly efficient liquid-phase exfoliation of α-zirconium phosphate, *J. Mater. Sci.* 57 (12) (2022) 6619–6628.

[41] K. Li, Ceramic membranes and membrane processes, in: Ceramic Membranes for Separation and Reaction, Wiley, 2007.

[42] A.I. Orlova, M.I. Ojovan, Ceramic mineral waste-forms for nuclear waste immobilization, *Materials* 12 (16) (2019) 2638.

[43] H. Jin, M.B. Ansari, S.E. Park, Mesoporous MFI zeolites by microwave induced assembly between sulfonic acid functionalized MFI zeolite nanoparticles and alkyltrimethylammonium cationic surfactants, *Chem. Commun.* 47 (26) (2011) 7482–7484.

[44] T. Suzuki, T. Okuhara, Change in pore structure of MFI zeolite by treatment with NaOH aqueous solution, *Microporous Mesoporous Mater.* 43 (1) (2001) 83–89.

[45] C.D. Lago, H.P. Decolatti, L.G. Tonutti, B.O. Dalla Costa, C.A. Querini, Gas phase glycerol dehydration over H-ZSM-5 zeolite modified by alkaline treatment with Na_2CO_3, *J. Catal.* 366 (2018) 16–27.

[46] J.C. Groen, J.A. Moulijn, J. Pérez-Ramírez, Desilication: on the controlled generation of mesoporosity in MFI zeolites, *J. Mater. Chem.* 16 (22) (2006) 2121–2131.

[47] E. Dib, I.M. Costa, G.N. Vayssilov, H.A. Aleksandrov, S. Mintova, Complex H-bonded silanol network in zeolites revealed by IR and NMR spectroscopy combined with DFT calculations, *J. Mater. Chem. A* 9 (48) (2021) 27347−27352.
[48] D.R. Tallant, B.C. Bunker, C.J. Brinker, C.A. Balfe, Raman spectra of rings in silicate materials, *MRS Online Proc. Libr.* 73 (1) (1986) 261−267.
[49] J.P. Zhai, Z.K. Tang, Z.M. Li, I.L. Li, F.Y. Jiang, P. Sheng, X.J. Hu, Carbonization mechanism of tetrapropylammonium-hydroxide in channels of $AlPO_4$-5 single crystals, *Chem. Mater.* 18 (6) (2006) 1505−1511.
[50] L. Qian, H.F. Zhang, Controlled freezing and freeze drying: a versatile route for porous and micro-/nano-structured materials, *J. Chem. Technol. Biotechnol.* 86 (2) (2011) 172−184.
[51] S.J. Milne, H. Mostaghaci, The influence of different drying conditions on powder properties and processing characteristics, *Mater. Sci. Eng. A* 130 (2) (1990) 263−271.
[52] Q.H. Cheng, S. Debnath, E. Gregan, H.J. Byrne, Ultrasound-assisted SWNTs dispersion: effects of sonication parameters and solvent properties, *J. Phys. Chem. C* 114 (19) (2010) 8821−8827.